

# Linear Instability of Viscous Parallel Shear Flows: Revisiting the No-slip Condition

John O. Dabiri\* and Anthony Leonard

Graduate Aerospace Laboratories and Department of Mechanical and Civil Engineering,  
California Institute of Technology, Pasadena, CA 91125, United States

(Dated: December 14, 2023)

Linear stability analysis currently fails to predict turbulence transition in canonical viscous flows. We show that an alternative model of flow at solid walls produces linear instabilities that could be sufficient to explain turbulence transition. The discovered instabilities satisfy the no-slip condition after a brief transient; hence, their behavior is empirically indistinguishable from the classical no-slip condition. These results suggest that the no-slip condition may be an overly simplified model of fluid-solid interface physics, thereby limiting the fidelity of stability predictions.

Keywords: hydrodynamic stability, transition, turbulence

*Introduction.*—A predictive model of the transition from laminar flow to turbulence in viscous parallel shear flows has remained elusive since seminal empirical observations of turbulence transition in the late 19th century [1]. One of the earliest and most thoroughly explored approaches to this problem examines the linear stability of the Navier-Stokes equations when subjected to small velocity perturbations [2]. Evaluation of the temporal growth of the perturbations typically proceeds by solution of the Orr-Sommerfeld eigenvalue equation (see Supp. Materials [3]), which depends on the Reynolds number of the flow,  $Re = U_0 L / \nu$ , where  $U_0$  and  $L$  are characteristic flow speed and length scales, respectively, and  $\nu$  is the kinematic viscosity of the fluid. Velocity perturbations are constrained to satisfy a no-slip condition at the fluid-solid interfaces. The eigenvalue problem conventionally incorporates this requirement with the homogeneous boundary condition:

$$\tilde{\mathbf{u}}(\mathbf{x}_{\text{wall}}, t) = 0 \quad (1)$$

where  $\tilde{\mathbf{u}}$  is the perturbation velocity vector amplitude and  $\mathbf{x}_{\text{wall}}$  is the location of the fluid-solid interfaces.

The aforementioned analysis predicts that plane Couette flow is stable to all two-dimensional linear perturbations at all Reynolds numbers [4]. This prediction is contradicted by empirical observations of transition to turbulence at channel Reynolds numbers as low as  $Re \approx 360$  [2]. The analysis method similarly finds no linear instability to account for the observed transition of Hagen-Poiseuille pipe flow to turbulence at a Reynolds number  $Re \approx 2000$ . For planar Poiseuille flow, linear stability analysis does identify a single unstable eigenmode, which first appears at a Reynolds number  $Re \approx 5772$  [5]. In practice, however, transition to turbulence is observed to occur at significantly lower Reynolds numbers  $Re \approx 1000$ . Moreover, the

growth rate associated with the unstable eigenvalue  $\hat{\omega}$  at  $Re \approx 5772$  is relatively weak, i.e., its imaginary part  $\text{Im}[\hat{\omega}] \approx 0.0037$ . The associated unstable eigenmode may therefore be insufficient to trigger turbulence.

This apparent inability of linear stability theory to accurately predict turbulence transition in a variety of viscous parallel shear flows has motivated the exploration of alternative frameworks to explain and possibly predict turbulence transition. These include consideration of finite-sized velocity perturbations [6], nonlinear transition processes [7], and transient growth mechanisms such as those associated with non-normality of the Orr-Sommerfeld eigenvalue equation [8].

We show that linear stability analysis is sufficient to predict the occurrence of turbulence transition in each of the aforementioned shear flows. To do so, we consider a more general ansatz for the boundary condition in the Orr-Sommerfeld equation, of which the no-slip condition is a limiting case. Evaluation of the associated parameter space of this boundary condition reveals strongly unstable eigenmodes that appear at Reynolds numbers below the empirically observed transition to turbulence. The results therefore allow for transition to turbulence without the need to appeal to nonlinear or transient growth processes. Instead, they suggest a re-examination of the no-slip condition as a sufficiently accurate model of the fluid-solid interface physics.

*Generalized boundary condition.*—We replace the streamwise component of the no-slip condition in equation (1) with a more general, homogeneous boundary condition that depends on the shear rate of the velocity perturbation at the wall:

$$\tilde{u}(\mathbf{x}_{\text{wall}}, t) \mp S \tilde{u}'(\mathbf{x}_{\text{wall}}, t) = 0 \quad (2)$$

where  $\tilde{u}$  is the streamwise component of the velocity perturbation amplitude,  $\tilde{u}' = \partial \tilde{u} / \partial y$  for the plane Couette and Poiseuille flows,  $\tilde{u}' = \partial \tilde{u} / \partial r$  for the Hagen-Poiseuille pipe flow,  $S$  is a characteristic slip length constant, and the sign  $\mp$  applies to the wall at  $y$  (or  $r$ ) = 1 and  $y = -1$ , respectively.

\* Correspondence email address: jodabiri@caltech.edu

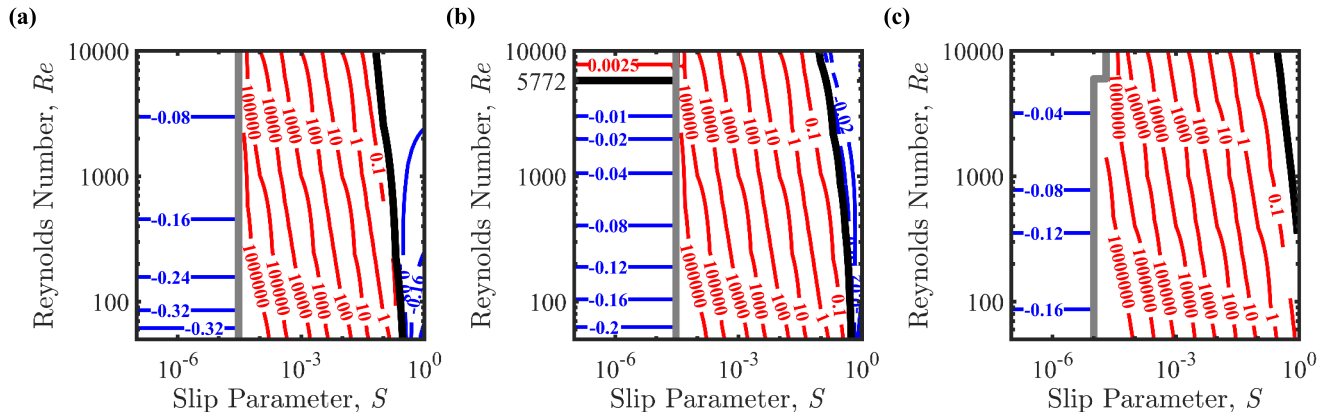


Figure 1. Contour maps of the maximum Orr-Sommerfeld eigenvalue imaginary part  $\mathbb{I}[\hat{\omega}]$  versus slip parameter  $S$  and Reynolds number  $Re$  for (a) plane Couette flow, (b) plane Poiseuille flow, and (c) Hagen-Poiseuille pipe flow. Blue contours indicate regions of linear stability, and red contours indicate regions of linear instability. Black contours indicate neutral stability boundaries. The Reynolds number  $Re \approx 5772$  of the single unstable eigenmode in plane Poiseuille flow for  $S = 0$  is indicated on the ordinate axis in panel (b). Vertical gray lines correspond to a discontinuous change in predicted hydrodynamic stability, reflecting the inability of the Chebyshev expansion ( $N = 400$ ) to resolve unstable eigenmodes for values of slip parameter  $S$  below the gray line. See Supp. Materials for details of each calculation.

Physically, the boundary condition in equation (2) requires that any non-zero perturbation velocity at the wall is in the same direction as the corresponding shear exerted on the fluid by the wall. While it is similar in form to the Navier slip boundary condition [9], a key distinction in the present case is that this boundary condition applies only to velocity *perturbations*. The base flow is assumed to exhibit a no-slip condition.

This generalized boundary condition (2) reduces to the no-slip condition (1) when the slip parameter  $S = 0$ . The no-slip condition is also satisfied by velocity perturbations with non-zero values of the slip parameter  $S$  if the corresponding wall-normal gradient of streamwise flow speed is zero at the wall, i.e.,  $\tilde{u}'(\mathbf{x}_{\text{wall}}, t) = 0$ . Finally, we will see that additional eigenmodes corresponding to  $S > 0$  also satisfy the no-slip condition except for periodic, discrete wall displacements on the order of the eigenmode wavelength [10]. This latter scenario corresponds to strongly unstable eigenmodes at subcritical Reynolds numbers, i.e., at Reynolds numbers consistent with empirical observations of turbulence transition.

*Linear stability maps.*—The Orr-Sommerfeld eigenvalue equation was solved for plane Couette flow, plane Poiseuille flow, and Hagen-Poiseuille pipe flow using Chebyshev collocation ([7, 11], see Supp. Materials for governing equations and Matlab implementations [3]). The boundary condition in equation (2) was evaluated for values of the slip parameter  $S = 0$  and ranging from  $S = 10^{-7}$  to  $S = 1$  in 10 equally-spaced increments per decade. The Reynolds number was varied from  $Re = 50$  to  $Re = 10,000$  in increments of 10.

For combinations of slip parameter  $S$  and Reynolds

number  $Re$  spanning this range, figure 1 plots contours of the maximum eigenvalue imaginary part, i.e.,  $\mathbb{I}[\hat{\omega}]$ , for Orr-Sommerfeld solutions corresponding to plane Couette flow, plane Poiseuille flow, and Hagen-Poiseuille pipe flow, respectively [12]. Positive contour values (red) indicate regions of linear instability, i.e., exponential temporal growth of the initial velocity perturbation at a rate proportional to  $\mathbb{I}[\hat{\omega}]$ . Negative contour values (blue) indicate regions of linear stability; neutral stability boundaries are indicated in black.

For values of slip parameter  $S$  approaching zero, the linear stability maps are each consistent with the results of conventional linear stability analyses using equation (1) as the boundary condition for velocity perturbations. Specifically, both the plane Couette flow and the Hagen-Poiseuille pipe flow indicate linear stability of the flow (i.e.,  $\mathbb{I}[\hat{\omega}] < 0$ ) for all Reynolds numbers investigated. The plane Poiseuille flow is also in agreement with previous studies for  $S$  approaching zero, with a single unstable eigenmode appearing between  $Re = 5770$  and  $Re = 5780$  [5].

However, a striking discontinuity is observed in each of the linear stability maps as the slip parameter  $S$  is increased above a critical threshold (i.e., vertical gray lines). For values of slip parameter greater than this threshold  $S_{crit}$ , we observe a region of linear instability spanning up to four decades in  $S$ . These strongly unstable eigenmodes—with growth rates  $\mathbb{I}[\hat{\omega}]$  exceeding  $\mathcal{O}(10^7)$  in some cases—appear at all Reynolds numbers investigated, making them potentially relevant to the process of turbulence transition.

The apparent lack of unstable eigenmodes for values of slip parameter  $S < S_{crit}$  is an artifact of the lim-

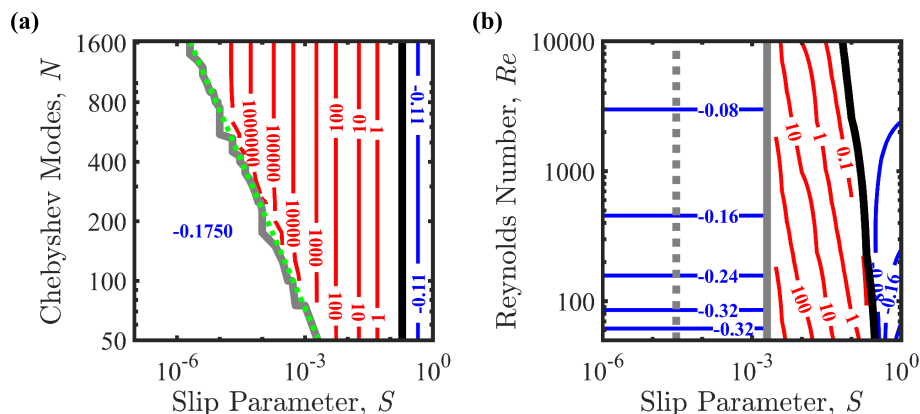


Figure 2. (a) Contour map of the maximum Orr-Sommerfeld eigenvalue imaginary part  $\mathbb{I}[\hat{\omega}]$  versus slip parameter  $S$  and number of Chebyshev modes  $N$  for plane Couette flow at  $Re = 360$  and wavenumbers  $(\alpha, \beta) = (1, 0)$ . Blue contours indicate regions of linear stability, and red contours indicate regions of linear instability. Neutral stability boundary is indicated by black line. Discontinuity in stability is indicated by gray curve. The location of the stability discontinuity shifts to lower values of the slip parameter  $S$  as  $N$  increases, reflecting the ability to resolve unstable eigenmodes with decreasing slip length scale  $S$  for increasing numbers of modes  $N$  used in the Chebyshev expansion. The minimum number of Chebyshev modes  $N_{min}$  required to resolve unstable eigenmodes for a given slip parameter  $S$  is well approximated by  $N_{min} \approx 2.3 S^{-1/2}$  (i.e., green dotted line). (b) Contour map of the maximum Orr-Sommerfeld eigenvalue imaginary part versus slip parameter  $S$  and Reynolds number  $Re$  computed using  $N = 50$  Chebyshev modes. The stability discontinuity (i.e., gray dotted line) from figure 1(a), computed using  $N = 400$  Chebyshev modes, is reproduced to illustrate the upward shift in the threshold value of the slip parameter  $S_{crit}$  corresponding to the stability discontinuity when fewer Chebyshev modes are used.

ited spatial resolution of the Chebyshev expansion using a finite number of modes. To illustrate this, figure 2(a) plots contours of the maximum Orr-Sommerfeld eigenvalue imaginary part  $\mathbb{I}[\hat{\omega}]$  versus slip parameter  $S$  and number of Chebyshev modes  $N$ , for the case of plane Couette flow at  $Re = 360$  and wavenumbers  $(\alpha, \beta) = (1, 0)$ . As in figure 1(a), blue and red contours indicate regions of linear stability and instability, respectively. The neutral stability boundary is indicated by a black line, and the discontinuity in stability is indicated by the gray curve. Eigenvalue contours to the right of the gray curve are oriented vertically, indicating that the corresponding eigenvalues are insensitive to the number of Chebyshev modes used to solve the Orr-Sommerfeld equation. This suggests that the computed eigenmodes are not spurious artifacts of the numerical method (cf. [13]). By contrast, the location of the stability discontinuity shifts to lower values of the slip parameter  $S$  as the number of Chebyshev modes used to compute the eigenmodes increases. This boundary reflects the finite spatial resolution of the Chebyshev representation of unstable eigenmodes for finite mode numbers  $N$ . As the number of Chebyshev modes is increased, unstable eigenmodes with smaller slip length scale  $S$  are successfully resolved. The minimum number of Chebyshev modes  $N_{min}$  required to resolve unstable eigenmodes for a given slip parameter  $S$  is well approximated by  $N_{min} \approx 2.3 S^{-1/2}$  (i.e., green dotted line).

Figure 2(b) provides a complementary illustration of

this trend, showing the linear stability map computed using  $N = 50$  Chebyshev modes. For comparison with the stability map computed using  $N = 400$  Chebyshev modes in figure 1(a), the stability discontinuity (i.e., gray dotted line) from that plot is reproduced here. The results highlight the need to implement Chebyshev collocation with a sufficient number of collocation points to resolve the distinct shape of unstable eigenmode profiles in close proximity to the wall. Calculations using an insufficient number of Chebyshev modes erroneously predict the absence of any unstable modes. In light of the trend  $N_{min} \sim S^{-1/2}$ , the number of Chebyshev modes required to resolve unstable eigenmodes becomes prohibitive as the conventional no-slip condition is approached (i.e.,  $S \rightarrow 0$ ). To be sure, a similar resolution challenge will be faced by other numerical methods.

*Asymptotic analysis of Couette flow.*—To further analyze the discovered unstable eigenmodes while circumventing the aforementioned numerical resolution challenges, we conducted an asymptotic analysis of plane Couette flow in the limit of strongly unstable eigenmodes, i.e.,  $\mathbb{I}[\hat{\omega}] \gg 1$  (see Appendix D in Supp. Materials [3]). This analysis predicts that the unstable eigenmode growth rate scales with slip parameter  $S$  and Reynolds number  $Re$  as  $\mathbb{I}[\hat{\omega}] \sim S^{-2} Re^{-1}$ . Moreover, the unstable plane Couette eigenmode amplitude components have the predicted asymptotic form

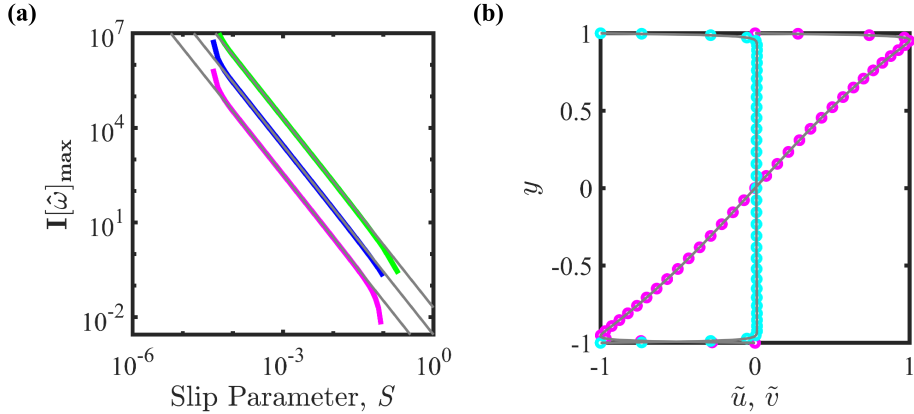


Figure 3. (a) Maximum unstable eigenvalues of plane Couette flow plotted versus slip parameter  $S$ . Thick colored curves are computed using Chebyshev collocation ( $N = 400$ ) for  $Re = 50$  (green),  $Re = 360$  (blue), and  $Re = 3000$  (magenta). Thin gray lines are corresponding analytical model prediction  $\mathbb{I}[\hat{\omega}] \sim S^{-2} Re^{-1}$ . (b) Streamwise ( $\tilde{u}$ , cyan) and wall-normal ( $\tilde{v}$ , magenta) components of unstable eigenmode amplitude profiles computed using Chebyshev collocation ( $N = 400$ ,  $Re = 360$ ,  $S = 1 \times 10^{-2}$ , and  $\alpha = 1$ ). Corresponding eigenmode profiles predicted by asymptotic analyses in equations (3) and (4) are shown in superimposed thin gray curves.

$$\tilde{u}(y) \approx (i/\alpha) \left[ (1/S)e^{(y-1)/S} + (1/S)e^{-(y+1)/S} - \frac{\alpha \cosh \alpha(y+1)}{\sinh 2\alpha} - \frac{\alpha \cosh \alpha(y-1)}{\sinh 2\alpha} \right] + \mathcal{O}(S) \quad (3)$$

$$\tilde{v}(y) \approx e^{(y-1)/S} - e^{-(y+1)/S} - \frac{\sinh \alpha(y+1)}{\sinh 2\alpha} - \frac{\sinh \alpha(y-1)}{\sinh 2\alpha} + \mathcal{O}(S) \quad (4)$$

Figure 3 compares the predictions of the asymptotic analysis with the calculations of plane Couette flow using Chebyshev collocation with  $N = 400$ . The agreement is excellent for both the maximum unstable eigenvalues (panel (a)) and the shape of each component of the unstable eigenmode (panel (b)). These results further support the conclusion that the discovered unstable eigenmodes are not spurious numerical artifacts.

*Example unstable eigenmodes.*—We examined a subset of the discovered unstable, subcritical eigenmodes in further detail using the asymptotic model for plane Couette flow described above. Figure 4 illustrates the behavior of unstable eigenmodes at  $Re = 360$  and  $S = 1 \times 10^{-2}$ , for streamwise wavenumbers  $\alpha = 1$  and 8. These unstable eigenmodes have growth rates  $\mathbb{I}[\hat{\omega}] = 27.2$  and 2.9, respectively. Each growth rate corresponds to a pair of left- and right-traveling eigenmodes with phase speeds  $\mathbb{R}[\hat{\omega}]/\alpha \rightarrow \pm 1$ .

For both wavenumbers, the streamwise pressure gradient is confined to the near-wall region, and the sign of the gradient alternates in a banded spatial structure matching the streamwise wavenumber of the eigenmode

(figure 4(a, c)). The magnitude of the pressure gradients increases exponentially according to the eigenmode growth rate, and the sign of the pressure gradient reverses periodically according to the eigenmode temporal frequency at times  $t = (\pi/2 + \pi j)/\mathbb{R}[\hat{\omega}]$ , where  $j$  is an integer (see Movies 1 and 2 in Supp. Materials [3]). Qualitatively similar results were observed up to a wavenumber  $\alpha \approx 10^4$ . At higher wavenumbers, the flow was found to be stable for all Reynolds numbers.

The fluid particles on each wall at  $y = \pm 1$  correspondingly migrate along the wall to the nodes of the eigenmodes at  $x = 2\pi j/\alpha$  (figure 4(b, d)). Following this initial transient migration, particles remain stationary in the reference frame of the wall, with the possible exception of periodic, rapid migration to an adjacent node as the local pressure gradient switches sign (e.g., at time  $t = \pi/2\mathbb{R}[\hat{\omega}]$  and  $t = 3\pi/2\mathbb{R}[\hat{\omega}]$  in panel (d). See also Movies 3 and 4 in Supp. Materials [3]).

After the initial eigenmode transient at time  $0 < t < \pi/128$ , the flow kinematics exhibited in figure 4(b, d) are physically consistent with the no-slip condition, i.e., fluid particles remain stationary on the walls. This is despite these eigenmodes arising from the generalized boundary condition (2) with  $S > 0$ . In light of this result, there appears to be no *a priori* justification to favor the boundary condition in equation (1) over the one in equation (2) as a more accurate model of the eigenmode flow physics.

To the contrary, the present analysis demonstrates that a framework in which the conventional no-slip condition is relaxed can reveal new physics that may help to resolve longstanding questions regarding the process of turbulence transition. Specifically, the discovered linearly unstable eigenmodes imply the presence of distinct

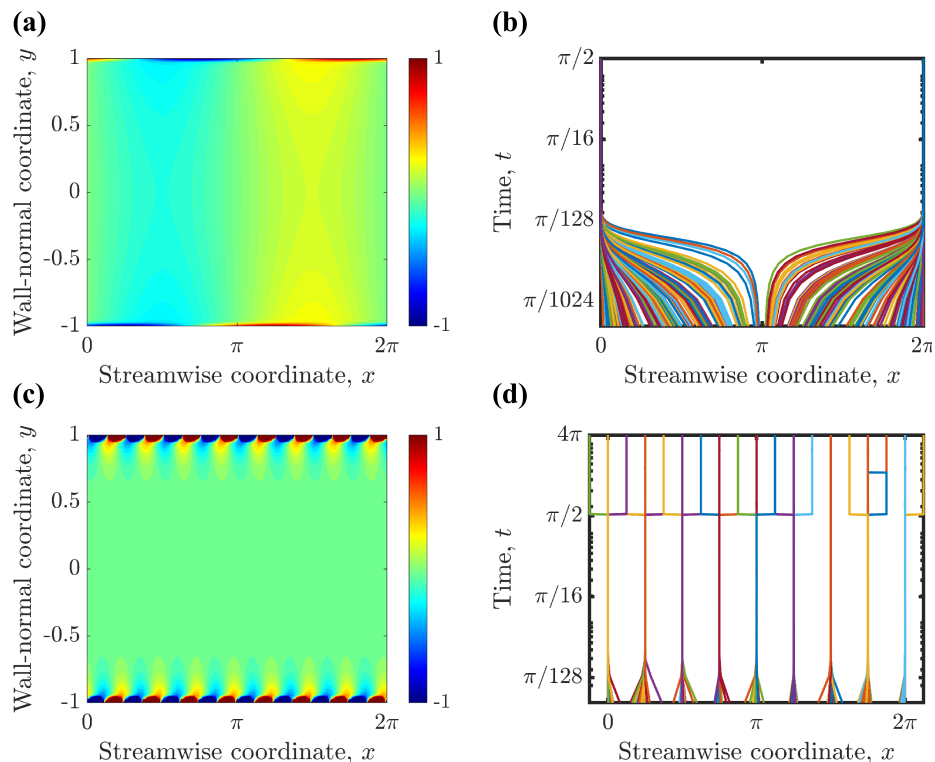


Figure 4. Example unstable eigenmodes at  $Re = 360$  and  $S = 1 \times 10^{-2}$ . *Left:* Contours of normalized streamwise pressure gradient  $\partial p / \partial x$  at time  $t = 0$  for streamwise wavenumber  $\alpha = 1$  (panel a) and  $\alpha = 8$  (panel c). *Right:* Corresponding  $x - t$  diagrams of Lagrangian trajectories of 256 fluid particles initialized along the walls of the plane Couette flow (i.e.,  $y = \pm 1$ ) at random locations in the range  $0 < x < 2\pi$ .

flow kinematics that may be observable in experiments that confirm their existence, e.g., the periodic, discrete shifts of fluid particles along the wall over distances on the order of the eigenmode wavelength (figure 4(b, d)). Moreover, the finding that linear instabilities vanish for streamwise wavenumbers  $\alpha \gtrsim 10^4$  implies a possible

strategy to suppress turbulence transition by driving incipient instabilities toward extremely high wavenumbers. The present theoretical framework can guide experimental efforts to test these predictions.

We thank M. Malik for discussion of the pipe flow calculations and M. K. Fu for manuscript feedback. J.O.D. was supported by the U.S. National Science Foundation.

- 
- [1] O. Reynolds, *Philos. Trans. R. Soc. A* **174**, 935 (1883).  
[2] P. G. Drazin and W. H. Reid *Hydrodynamic Stability* (Cambridge Mathematical Library, Cambridge, 2004).  
[3] See Supplemental Material at [URL will be inserted by publisher] for methods and movies.  
[4] A. Davey, *J. Fluid Mech.* **57**, 369 (1973).  
[5] S. A. Orzag, *J. Fluid Mech.* **50**, 689 (1971).  
[6] S. A. Orzag and L. C. Kells, *J. Fluid Mech.* **96**, 159 (1980).  
[7] P. J. Schmid and D. S. Henningson *Stability and Transition in Shear Flows* (Springer, New York, 2001).  
[8] L. N. Trefethen, A. E. Trefethen, S. C. Reddy and T. A. Driscoll, *Science* **261**, 578 (1993).  
[9] E. Lauga, M. P. Brenner and H. A. Stone *Springer Handbook of Experimental Fluid Mechanics, Ch. 19* (Springer, Berlin, Heidelberg, 2007).  
[10] While this discussion focuses on the case of real-valued slip parameter  $S$ , we have observed similar results for complex  $S$ . In the latter case, a phase difference exists between the perturbation wall slip and the wall-normal gradient of the perturbation wall slip.  
[11] M. Malik and M. Skote, *Comp. Fluids* **192**, 104267 (2019).  
[12] Similar contour maps of the second-largest eigenvalue are provided in Appendix C of Supp. Materials for reference.  
[13] P. T. Dawkins, S. R. Dunbar and R. W. Douglass, *J. Comp. Phys.* **147**, 441 (1998).

**SUPPLEMENTAL MATERIAL**

**Appendix A: Orr-Sommerfeld Equations**

*Plane Couette and Plane Poiseuille Flow*

Following [7], we consider velocity perturbations of the general Cartesian form

$$\mathbf{u}(x, y, z, t) = \mathbb{R}[\tilde{\mathbf{u}}(y)e^{i(\alpha x + \beta z - \omega t)}] \quad (\text{A.1})$$

where the Cartesian components of the velocity vector are  $\mathbf{u} = u\hat{\mathbf{i}} + v\hat{\mathbf{j}} + w\hat{\mathbf{k}}$  in the streamwise (i.e.,  $\hat{\mathbf{i}}$ ), wall-normal (i.e.,  $\hat{\mathbf{j}}$ ), and transverse (i.e.,  $\hat{\mathbf{k}}$ ) directions. The temporal evolution of the perturbations is examined by treating the spatial wavenumbers as  $\alpha, \beta \in \mathbb{R}$  and the frequency as  $\omega = \alpha c$ , where  $c \in \mathbb{C}$  is the complex phase speed of the perturbation. The stability of perturbations of a given spatial wavenumber is evaluated by solving the Orr-Sommerfeld equation:

$$\left[(-i\omega + i\alpha U)(\mathcal{D}^2 - k^2) - i\alpha U'' - \frac{1}{Re}(\mathcal{D}^2 - k^2)^2\right]\tilde{v} = 0 \quad (\text{A.2})$$

where  $k^2 = \alpha^2 + \beta^2$ , and  $Re = U_0 L / \nu$  is the Reynolds number. Here,  $U_0$  is taken as the maximum velocity of the base flow in the domain, and  $L$  is the half-width of distance between the solid walls of the Couette or Poiseuille flow. The operator  $\mathcal{D}$  and the prime both denote a derivative with respect to the wall-normal  $y$ -coordinate direction.

For plane Couette flow, the base flow is given by  $U(y) = y$  on the domain  $-1 \leq y \leq 1$ . For plane Poiseuille flow, the base flow is given by  $U(y) = 1 - y^2$  on the domain  $-1 \leq y \leq 1$ . Equation (A.2) is solved using the boundary condition  $\tilde{v} = 0$  at  $y = \pm 1$  (i.e., no flow penetration at the solid walls), along with the generalized boundary condition for the streamwise perturbation component  $\tilde{u}$  in equation (2) to replace the conventional no-slip condition. Given the form of velocity perturbation in equation (A.1), and using  $\tilde{u} = (i/\alpha)\mathcal{D}\tilde{v}$  from the continuity equation, the generalized boundary condition for  $\tilde{u}$  can be written in terms of the normal velocity  $\tilde{v}$  as

$$\frac{i}{\alpha}\mathcal{D}\tilde{v} \mp \frac{i}{\alpha}S\mathcal{D}^2\tilde{v} = 0 \quad \text{for } y = \pm 1 \quad (\text{A.3})$$

*Hagen-Poiseuille Pipe Flow*

Following [11], we consider velocity perturbations in cylindrical coordinates of the form

$$\mathbf{u}(x, r, \theta, t) = \mathbb{R}[\tilde{\mathbf{u}}(r)e^{i(\alpha x + n\theta - \omega t)}] \quad (\text{A.4})$$

where  $(x, r, \theta)$  are the axial, radial, and azimuthal directions, respectively, and  $n$  is the azimuthal wavenumber. The Orr-Sommerfeld equations can be expressed as

$$\begin{aligned} i(\alpha U - \omega)(\mathcal{D}\tilde{u} - i\alpha\tilde{v}) &= -i\alpha U'\tilde{u} - (U'' + U'\mathcal{D})\tilde{v} + \frac{1}{Re}\left(\Delta(\mathcal{D}\tilde{u} - i\alpha\tilde{v}) - 2inr^{-2}\tilde{\eta}\right) \\ i(\alpha U - \omega)[\mathcal{D}(r\tilde{w}) - in\tilde{v}] &= -i\alpha r U'\tilde{w} + \frac{1}{Re}\left(\bar{\Delta}[\mathcal{D}(r\tilde{w}) - in\tilde{v}]\right) \\ i(\alpha U - \omega)\tilde{\eta} &= -inU'r^{-1}\tilde{v} + \frac{1}{Re}\left(\Delta\eta + 2nr^{-2}(\alpha\tilde{v} + i\mathcal{D}\tilde{u})\right) \end{aligned} \quad (\text{A.5})$$

where  $\Delta = [\mathcal{D}^2 + r^{-1}\mathcal{D} - r^{-2}(d+1)]$ ,  $\bar{\Delta} = [\mathcal{D}^2 - r^{-1}\mathcal{D} - r^{-2}(d-1)]$ ,  $\tilde{\eta} = i(nr^{-1}\tilde{u} - \alpha\tilde{w})$ ,  $d = n^2 + \alpha^2 r^2$ , and the operator  $\mathcal{D}$  and the prime both denote a derivative with respect to the radial direction. The base flow for Hagen-Poiseuille pipe flow is given by  $U(r) = 1 - r^2$  on the domain  $0 \leq r \leq 1$ .

The Orr-Sommerfeld equations are solved following [11] by using surrogate analytic functions  $(\phi, \Omega)$  that facilitate more straightforward implementation of the generalized boundary condition in equation (2) and regularity conditions on the axis of symmetry  $r = 0$ . The wall-normal velocity and vorticity are expressed in terms of these functions as

$$(\tilde{v}, \tilde{\eta}) = \begin{cases} (r^l \phi, r^l \Omega), & n \neq 0 \\ (r \phi, r \Omega), & n = 0 \end{cases} \quad (\text{A.6})$$

where  $l = |n| - 1$ . The no-penetration boundary condition is therefore given by  $\phi = 0$  at  $r = 1$ .

Using continuity and the normal vorticity definition, the streamwise (i.e.,  $\tilde{u}$ ) velocity perturbation component is given by

$$\tilde{u} = \begin{cases} \frac{ir^{l+1}}{d} [\alpha(l+1)\phi + \alpha r \mathcal{D}\phi - n\Omega], & n \neq 0 \\ \frac{i}{\alpha} (2\phi + r \mathcal{D}\phi), & n = 0 \end{cases} \quad (\text{A.7})$$

From equations (2) and (A.7), the generalized boundary condition for the streamwise velocity component at the wall ( $r = 1$ ) is

$$\begin{aligned} [(a_1 + a_3 + a_6)\mathcal{D} + a_4 \mathcal{D}^2]\phi + [(a_2 + a_7) + a_5 \mathcal{D}]\Omega &= 0, & n \neq 0 \\ [(a_1^0 + a_2^0)\mathcal{D} + a_3^0 \mathcal{D}^2]\phi &= 0, & n = 0 \end{aligned} \quad (\text{A.8})$$

where

$$\begin{aligned} a_1 &= \frac{i\alpha}{d} \\ a_2 &= -\frac{in}{d} \\ a_3 &= -\frac{S i \alpha (l+2)}{d} \\ a_4 &= -\frac{S i \alpha}{d} \\ a_5 &= \frac{S i n}{d} \\ a_6 &= -S \alpha \left[ \frac{i(l+1)d - 2i\alpha^2}{d^2} \right] \\ a_7 &= S n \left[ \frac{i(l+1)d - 2i\alpha^2}{d^2} \right] \\ a_1^0 &= \frac{i}{\alpha} \\ a_2^0 &= -3S \frac{i}{\alpha} \\ a_3^0 &= -S \frac{i}{\alpha} \end{aligned} \quad (\text{A.9})$$

## Appendix B: Numerical Solution

The Orr-Sommerfeld eigenvalue equations were solved using Chebyshev collocation as formulated in plane Cartesian coordinates [7] and cylindrical coordinates [11]. Matlab implementations of the algorithm for each flow are provided in Appendix E.

The Matlab codes were verified by comparing the computed eigenvalues for the case  $S = 0$  (i.e., no-slip condition) to the tabulated eigenvalues for plane Couette and Poiseuille flows in [7], as well as the tabulated eigenvalues for Hagen-Poiseuille pipe flow in [11].

For each of the three flows (i.e., plane Couette flow, plane Poiseuille flow, and Hagen-Poiseuille pipe flow), 400 collocation points were used to compute each of the  $996 Re \times 66 S = 65,736$  total cases in the  $S - Re$  parameter space of figure 1. Wavenumbers were fixed at  $\alpha = 1$  and  $\beta = 0$  for plane Couette flow and plane Poiseuille flow, and  $\alpha = 1$  and  $n = 1$  for Hagen-Poiseuille pipe flow. These wavenumbers typically corresponded to the most unstable eigenmodes, but qualitatively similar results were observed for other wavenumbers. The eigenvalue with maximum imaginary part was recorded for each parameter set ( $S, Re$ ) studied. If the eigenvalue with second-largest imaginary part was within  $10^{-3}$  of the eigenvalue with largest imaginary part, the eigenvalues were treated as a combined pair for the purposes of subsequent analysis.

## Appendix C: Second-Largest Orr-Sommerfeld Eigenvalue Imaginary Part

Figure C.1 plots contours of the second-largest eigenvalue imaginary part. These results demonstrate that the predicted linear instability is not necessarily limited to a single eigenvalue with positive imaginary part.

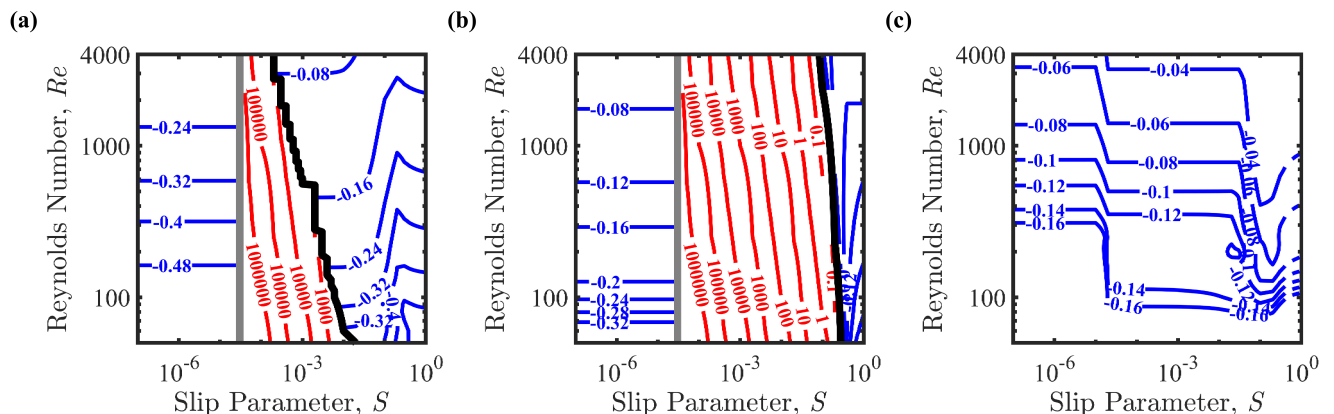


Figure C.1. Contour maps of the second-largest Orr-Sommerfeld eigenvalue imaginary part  $\Im[\hat{\omega}]$  versus slip parameter  $S$  and Reynolds number  $Re$  for (a) plane Couette flow, (b) plane Poiseuille flow, and (c) Hagen-Poiseuille pipe flow. Blue contours indicate regions of linear stability, and red contours indicate regions of linear instability. Black contours indicate neutral stability boundaries. Vertical gray lines correspond to a discontinuous change in predicted hydrodynamic stability, reflecting the inability of the Chebyshev expansion ( $N = 400$ ) to resolve unstable eigenmodes for values of slip parameter  $S$  below the gray line.



### Appendix D: Asymptotic Analysis of Unstable Couette Eigenmodes

The Orr-Sommerfeld equation for plane Couette flow can be written as

$$\frac{\partial}{\partial t} \nabla^2 \tilde{v} - \frac{1}{Re} \nabla^2 \nabla^2 \tilde{v} + i\alpha \nabla^2 \tilde{v} = 0 \quad (\text{D.1})$$

where  $\alpha$  is the axial wavenumber. The temporal behavior of linear velocity perturbations is given by  $\tilde{v} \sim e^{-i\omega t}$ , where the complex frequency  $\omega = \mathbb{R}[\omega] + i\mathbb{I}[\omega]$ .

We consider the limiting case of large, unstable eigenvalues, i.e.,  $\mathbb{I}[\hat{\omega}] \gg 1$ . To leading order, equation (D.1) can therefore be written as

$$\left( \mathbb{I}[\hat{\omega}] Re + \alpha^2 - \frac{\partial^2}{\partial y^2} \right) \nabla^2 \tilde{v} = 0 \quad (\text{D.2})$$

Equation (D.2) has leading order solutions of the form  $\tilde{v} \sim e^{\pm\kappa_1 y}$ ,  $e^{\pm\alpha y}$ , where  $\kappa_1 = \sqrt{\mathbb{I}[\hat{\omega}] Re + \alpha^2} \gg 1$ . The solutions must satisfy a no-penetration condition at the walls, i.e.,  $\tilde{v}(y = \pm 1) = 0$ . This boundary condition is satisfied for

$$\tilde{v}(y) = e^{\kappa_1(y-1)} - \frac{\sinh \alpha(y+1)}{\sinh 2\alpha} + \kappa_2 \left( e^{-\kappa_1(y+1)} + \frac{\sinh \alpha(y-1)}{\sinh 2\alpha} \right) \quad (\text{D.3})$$

since  $\tilde{v}(y = \pm 1) \sim \mathcal{O}(e^{-2\kappa_1}) \approx 0$ . The free parameter  $\kappa_2$  can be constrained by applying the boundary condition in equation (2) as formulated for plane Couette flow in equation (A.3). Specifically, at  $y = 1$ :

$$\frac{\kappa_1 - \alpha \frac{\cosh 2\alpha}{\sinh 2\alpha} + \frac{\alpha \kappa_2}{\sinh 2\alpha}}{\kappa_1^2 - \alpha^2} = S \quad (\text{D.4})$$

where terms of  $\mathcal{O}(e^{-2\kappa_1})$  or smaller have been neglected. Similarly, at  $y = -1$ :

$$\frac{-\frac{\alpha}{\sinh \alpha} - \kappa_1 \kappa_2 + \alpha \kappa_2 \frac{\cosh 2\alpha}{\sinh 2\alpha}}{\kappa_2(\kappa_1^2 - \alpha^2)} = -S \quad (\text{D.5})$$

Combining equations (D.4) and (D.5) gives  $\kappa_2 = \pm 1$ . The negative solution  $\kappa_2 = -1$  gives antisymmetric eigenmodes consistent with the opposite direction of travel of the walls at  $y = \pm 1$ . Substituting this solution for  $\kappa_2$  into the system of equations gives the approximation  $\kappa_1 \approx S^{-1}$ , or equivalently:

$$\mathbb{I}[\hat{\omega}] \sim S^{-2} Re^{-1} \quad (\text{D.6})$$

This predicted scaling is consistent with the unstable eigenvalues computed using Chebyshev collocation with  $N = 400$  in figure 3(a) for  $Re = 50, 360, \text{ and } 3000$ . The preceding asymptotic analysis also predicts that eigenmode profiles corresponding to large, unstable eigenvalues have the approximate shape given in equations (3) and (4). This prediction is in excellent agreement with the profiles computed using Chebyshev collocation, as shown in figure 3(b).